III

Particle production

8 Particle spectra

8.1 A thermal particle source: a fireball at rest

The longitudinally scaling limit in production of hadrons, section 6.4, applies at the RHIC and at higher collision energies. At the SPS and AGS energy ranges, table 5.1, it is natural to explore the other reaction picture, the full-stopping limit. In this case all *matter* and *energy* available in the collision of two nuclei is dumped into a localized fireball of hot matter. Even at the highest SPS energies many experimental results suggest that such a reaction picture is more appropriate than the $(1 + 1)$-dimensional-flow picture.

The $m_\perp$ spectra we have seen in Fig. 1.7 on page 20 provide a strong encouragement to analyze the collision region in terms of the formation of a thermalized fireball of dense hadronic matter. The high slopes seen strongly suggest that the dynamic development in the transverse direction is very important. The pattern of similarity seen for very different particles is what would be expected to occur in hadronization of a nearly static fireball, and thus this case will be the first one we explore. However, we note that this is solely an academic exercise since SPS results provide ample evidence for rather rapid $v \simeq 0.5c$ transverse expansion. One can recognize this important physical phenomenon only once the properties of the stationary fireball matter are fully understood.

We consider a space–time-localized region of thermal hadronic matter acting as a source of particles, yielding naturally a Boltzmann spectral distribution. The thermal equilibrium is strictly a local property, with different temperatures possible in different space–time domains. The necessity that there is also a local thermal pressure implies that a fireball is in general a dynamically evolving object with local flows of matter, which we shall study further below. The virtue of this model is that the spectra

130

and abundances of particles can be described in terms of a few parameters that can be measured.

The thermal analysis of the experimental results differs in many key aspects from the microscopic-transport methods introduced in section 6.1. These contain as inputs detailed reaction data and their extrapolations, including often enough hypothetical reaction cross sections and novel mechanisms without which the experimental results cannot be described completely. The attainment of thermal equilibrium is, in these calculations, a result of many complex reactions. For the N–N collisions the appearance of the thermal particle distributions in the final state is still inexplicable in terms of such dynamic microscopic models. For this reason alone, a microscopic dynamic approach cannot lead to an understanding of the thermalization of fireball matter. Moreover, since the physical thermalization processes are faster than those operating in present-day numerical transport codes, microscopic transport theory delays the thermalization of collision energy available in heavy ion reactions and thus will in general fail at predicting observables of interest which depend on (early and rapid) thermalization. As long as these issues are being studied, an empirical thermal model allowing for flow of matter and non-equilibrium abundances of particles offers considerable advantages for the understanding of experimental data.

We first aim to relate the experimental rapidity and transverse-mass spectra to the particle distribution of the fireball. We consider the differential particle-momentum distribution, e.g., near the surface of the fireball,

$$E \frac{d^3 N}{d^3 p} \equiv f(E, p_{\mathrm{L}}), \qquad (8.1)$$

where the presence of p_{L} in the argument reminds us that an emitted particle could remember the collision axis; the distribution need not be intrinsically spherically symmetric as is implied when only the energy of the particle is considered. The coefficient E is introduced in Eq. (8.1) for convenience, it assures that the quantity f is invariant under Lorentz transformations. This is understood on reexpressing the left-hand side of Eq. (8.1) in terms of the invariant variables $m_\perp$ and y. Given Eq. (5.4), at constant $p_\perp$, we find

$$dy = \frac{dp_{\mathrm{L}}}{E}. \qquad (8.2)$$

Since $p_\perp \, dp_\perp = m_\perp \, dm_\perp$, considering Eq. (5.5) the Lorentz-invariant momentum-space volume element is

$$\frac{d^3 p}{E} = dy \, m_\perp \, dm_\perp \, d\varphi. \qquad (8.3)$$

It is important to remember, looking at the spectra, that, while $p_\perp > 0$, we have $m_\perp > m$.

We consider at first as the intrinsic distribution the simplest exponential Boltzmann-type thermal shape:

$$f(E, p_L) \to CEe^{-\beta E} = Cm_\perp \cosh y \, e^{-\beta m_\perp \cosh y}, \tag{8.4}$$

with $C = gV/(2\pi^3)$ and Eq. (5.4) is used on the right-hand side to replace the particle energy by transverse mass and rapidity. Since we have a Lorentz-invariant distribution, a change of the frame of reference along the p_L axis, e.g., from the laboratory frame to the CM frame, is amounting to a shift along the rapidity y axis of the particle spectrum considered to be centered around the CM rapidity $y_{CM} = 0$, see section 5.3. The differential particle spectrum which we obtain is

$$\frac{d^2 N(y, m_\perp)}{m_\perp^2 \, dm_\perp \, dy} = C \int d\varphi \cosh y \, e^{-\beta m_\perp \cosh y}. \tag{8.5}$$

To obtain the transverse-mass spectra, we need to integrate Eq. (8.5) over the applicable rapidity acceptance (often referred to as 'rapidity window'):

$$\frac{1}{m_\perp} \frac{dN(y, m_\perp)}{dm_\perp} = C \int d\varphi \int_{y^-}^{y^+} dy \, m_\perp \cosh y \, e^{-\beta m_\perp \cosh y}. \tag{8.6}$$

For a wide (see below) rapidity window, we can extend the limit of the integration to infinity, since the argument is a rapidly decreasing exponential function. We use Eqs. (10.44) and (10.45) and obtain

$$K_1(z) = \int_0^\infty dt \, e^{-z \cosh t} \cosh t,$$
$$\to \left(\frac{\pi}{2z}\right)^{1/2} e^{-z} \left(1 + \frac{3}{8z} - \frac{15}{128z^2} \cdots \right). \tag{8.7}$$

We obtain for the full rapidity coverage

$$\frac{1}{m_\perp^{3/2}} \frac{dN(y, m_\perp)}{dm_\perp} \propto e^{-\beta m_\perp} \left(1 + \frac{3}{8\beta m_\perp} \cdots \right). \tag{8.8}$$

For a narrow rapidity window, $\delta y = y^+ - y^-$, surrounding y_{CM}, one simply substitutes, in the integral Eq. (8.6), $\cosh(\delta y/2)$ by 1 and the result is

$$\frac{1}{m_\perp} \frac{dN(y, m_\perp)}{dm_\perp} \propto e^{-\beta m_\perp}. \tag{8.9}$$

In both cases, Eqs. (8.8) and (8.9), we have a (nearly) exponential transverse-mass spectrum, provided that the preexponential factors in the spectra
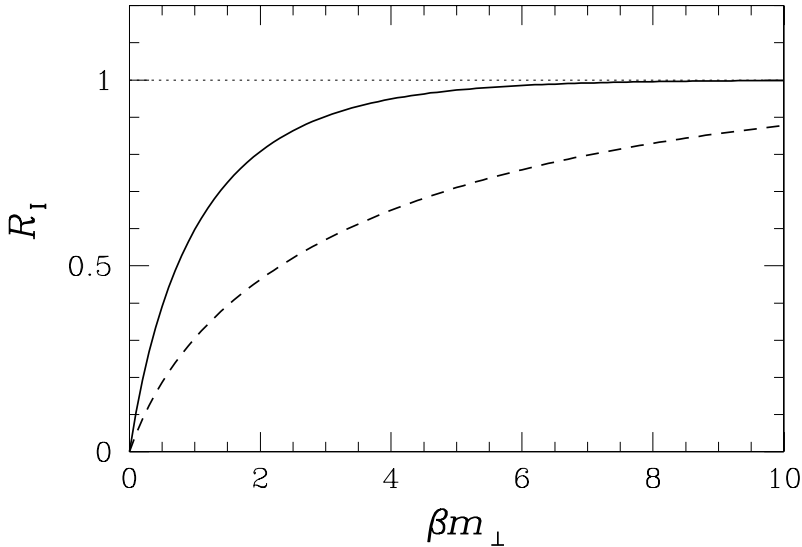
Fig. 8.1. The saturation of particle yield for a fireball at rest within a rapidity window: dashed line, $y^{\pm} = y_{CM} \pm 0.5$ and solid line $y^{\pm} = y_{CM} \pm 1$, as a function of $\beta m_{\perp}$; see the text for details.

are properly chosen. The result is not at all what one is naively tempted to use when one is fitting invariant cross sections, i.e., to simply take an exponential fit of the cross-section data: the choice is either to include the factor $1/m_{\perp}^{1/2}$ (compare with Fig. 8.9 and also Fig. 8.8), or to multiply by $1/m_{\perp}$ for a truly narrow rapidity window, as we see in Fig. 1.7 on page 20.

The question thus is that of how narrow the 'narrow' rapidity window must be for the factor to be as given in Eq. (8.9). We note that, in addition to the width of the typical experimental acceptance of 0.5–1 rapidity unit, one has to keep in mind that there is, in principle, a superposition of contributions to the spectra occurring due to longitudinal flow in the source, which effectively widens the rapidity acceptance domain. We show, in Fig. 8.1, the ratio

$$R_{\mathrm{I}} \equiv \frac{\int_{y_-}^{y_+} dy \, \cosh(y - y_{CM}) \, e^{-\beta m_{\perp} \cosh(y - y_{CM})}}{\int_{-\infty}^{+\infty} dy \, \cosh(y - y_{CM}) \, e^{-\beta m_{\perp} \cosh(y - y_{CM})}}, \tag{8.10}$$

of the rapidity integral Eq. (8.6) with the full rapidity coverage, as a function of $\beta m_{\perp}$. Results shown are for a rapidity window of one unit (dashed line, $y^{\pm} = y_{CM} \pm 0.5$) and two units (solid line, $y^{\pm} = y_{CM} \pm 1$) of rapidity, centered around y_{CM}.

We see that, for an experimental rapidity window of one unit (e.g., $-0.5 < y - y_{CM} < 0.5$) (dashed line) and for a typical 'high' transverse

mass $m_\perp \simeq 1.5$ GeV at $T \to T_\perp = 1/\beta = 230$–300 MeV, we would
have reached nearly 80%–90% of the full rapidity integral, justifying use
of a result with a full rapidity window coverage – note that adding in
smearing of flow (the solid line) means that more than 99% of the spectral
strength will be effectively included. Consequently, we find that the test
for applicability of Eq. (8.8) is $\beta m_\perp \cosh(\delta y/2) > 8$, with $\delta y/2$ comprising
an estimate of the flow.

We next consider the thermal rapidity spectra. We now integrate
Eq. (8.4) over the full range of transverse mass,

$$\frac{dN(y, m_\perp)}{dy} = C \int d\varphi \int_m^\infty dm_\perp \, m_\perp^2 \cosh y \; e^{-\beta m_\perp \cosh y}, \qquad (8.11)$$

to obtain the rapidity distribution shown in the top portion of Fig. 8.2,
for the case $m_\pi \lesssim \beta^{-1} < m_K$ (here $\beta^{-1} \equiv T = 160$ MeV).

The thin lines in Fig. 8.2 apply to spectra of massless particles, dashed
lines are for pions ($m = 138$ MeV), chain lines are for kaons ($m = 497$
MeV), and the thick solid line depicts data for nucleons ($m = 938$ MeV).
Since the experimental acceptance in $p_\perp$ cannot, for practical reasons,
begin with $p_\perp = 0$, we have also shown in Fig. 8.2 what happens to these
spectra when only particles with $p_\perp > p_\perp^{\min}$ are included, with minimum
momentum cutoffs shown at $p_\perp^{\min} = 0.3$, 0.5, and 1 GeV. We notice that,
when $p_\perp^{\min} < 0.5$ GeV, the maximum peak for massless particles is nearly
half as high as that for nucleons, and, correspondingly, the widths of the
distributions vary considerably with particle mass.

This change in relative abundance of the different particles increases
with $p_\perp^{\min}$ (we changed the scale of the drawing by a factor of three to
make the small remaining particle abundance more visible for $p_\perp^{\min} = 1$ GeV). The lighter particles disappear more rapidly and the relative
abundance of the heavier ones is increased in the sample. Moreover, all
shapes become increasingly more similar, resembling more and more the
nucleon spectrum. We note that for $p_\perp^{\min} = 0.3$, the half-width parameter,
for most particles, is within the range $0.6 < \sigma < 0.7$.

We see that, in the ideal situation of a thermal Boltzmann-like emitter,
the rapidity spectra of identified particles are very narrowly distributed
around the 'central' rapidity, with the distribution of the massive parti-
cles being narrower than that of lighter particles when all $p_\perp$ are included,
which difference disappears when the minimum $m_\perp$ for the different par-
ticles are (nearly) the same. Since the width of the rapidity spectra is
just half as large as was seen for the width for negative hadrons, h$^-$, see
Fig. 9.6, there must be some other contribution to the width, that is in
general believed to be the flow: the small source is not stationary, and its
size and all other properties evolve rapidly in time, an effect we address
in section 8.4.
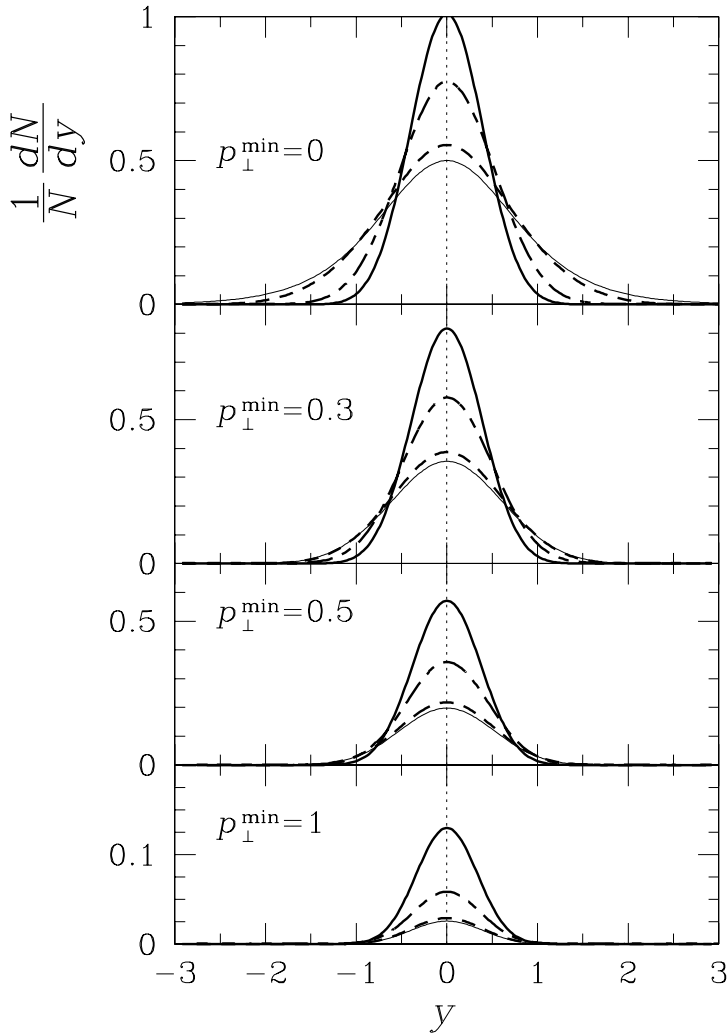
Fig. 8.2. Normalized thermal rapidity particle spectra (quantitative) for a Boltzmann (exponential) energy distribution with $\beta^{-1} = 160$ MeV and setting $y_{CM} = 2.92$ as appropriate for the highest SPS energy: massless particles (thin lines), pions (dashed lines), kaons (chain lines), and nucleons (solid lines). The effect of the minimum transverse-momentum cutoff on particle yield and shape of distribution is illustrated: we show $p_\perp^{min} > 0$, > 0.3, > 0.5, and > 1 GeV. Note the change of scale for the last (bottom) case.

Even though the above example of a thermal source is no more than a case study, we have learned much about the possible shape of the rapidity spectra of a well-defined, localized thermal source. This leads to the practical question of what spectral shape arises when identification of

particles is not possible. In such a case, one generally studies pseudorapidity distributions. We keep in mind that the relatively easily measurable pseudorapidity, Eqs. (5.24) and (5.25), arises from the rapidity, Eqs. (5.4) and (5.10), in the limit $m \to 0$, and thus, in cases when an appreciable yield of nucleons and even kaons is present, significant distortions in the spectra occur.

We now discuss this quantitatively and evaluate the shape of the thermal pseudorapidity distribution. Since η is not a good Lorentz variable, we study the specific example of the spectra in the laboratory frame in which the target is at rest and the projectile had $158A$ GeV. We take as the input spectrum the rapidity shape of the thermal source defined above in Eq. (8.11). To proceed with the change of variables, we need to express the CM energy and momentum of the distributions in terms of the laboratory pseudorapidity. Using Eq. (5.4),

$$E = m_\perp \cosh(y' - y_{\mathrm{CM}}) = E' \cosh y_{\mathrm{CM}} - p_{\mathrm{L}}' \sinh y_{\mathrm{CM}}, \tag{8.12a}$$

$$p_{\mathrm{L}} = m_\perp \sinh(y' - y_{\mathrm{CM}}) = p_{\mathrm{L}}' \cosh y_{\mathrm{CM}} - E' \sinh y_{\mathrm{CM}}. \tag{8.12b}$$

With the help of Eq. (5.24), we eliminate E' and p_{L}', using the pseudorapidity η' with reference to the laboratory frame, and $p_\perp$,

$$E = \sqrt{m^2 + p_\perp^2 \cosh^2 \eta'} \, \cosh y_{\mathrm{CM}} - p_\perp \sinh \eta' \, \sinh y_{\mathrm{CM}}, \tag{8.13a}$$

$$p_{\mathrm{L}} = p_\perp \sinh \eta' \, \cosh y_{\mathrm{CM}} - \sqrt{m^2 + p_\perp^2 \cosh^2 \eta'} \, \sinh y_{\mathrm{CM}}. \tag{8.13b}$$

We also obtain

$$\frac{1}{p_\perp} \frac{dp_{\mathrm{L}}}{d\eta'} = \cosh \eta' \cosh y_{\mathrm{CM}} - \frac{p_\perp \sinh \eta' \, \sinh y_{\mathrm{CM}} \cosh \eta'}{\sqrt{m^2 + p_\perp^2 \cosh^2 \eta'}}, \tag{8.14}$$

for the (frame-of-reference-dependent) integration Jacobian relating the CM longitudinal momentum and laboratory pseudorapidity (see Eq. (8.2) for comparison).

We now are ready to evaluate the pseudorapidity particle distribution. Proceeding in the same way as when we obtained Eq. (8.11), i.e., integrating over the azimuthal angle and the transverse momentum, and effecting the change of the integration variable from longitudinal momentum to pseudorapidity, we obtain, in the laboratory frame, the pseudorapidity distribution

$$\frac{dN}{d\eta'} \equiv 2\pi \int dp_\perp \, p_\perp^2 \left(\frac{dp_{\mathrm{L}}'}{p_\perp \, d\eta'} \right) \frac{f(E, p_{\mathrm{L}})}{E}. \tag{8.15}$$

The arguments of the distribution are as given in Eqs. (8.13a) and (8.13b) and the volume element is given by Eq. (8.14).

Equipped with this result, we can explore quantitatively the case of the exponential, thermal-like distribution, Eq. (8.4). The explicit form of the laboratory pseudorapidity distribution, including a necessary Lorentz contraction factor $(\cosh y_{\mathrm{CM}})^{-1}$ arising from the Lorentz transformation of the volume V of the source, takes the form

$$\frac{dN}{d\eta'} = 2\pi C \int_{p_{\perp}^{\mathrm{min}}}^{\infty} dp_{\perp} \; p_{\perp}^2 \, e^{-\beta\left[\cosh y_{\mathrm{CM}}\sqrt{m^2+p_{\perp}^2\cosh^2\eta'}-p_{\perp}\sinh y_{\mathrm{CM}}\sinh\eta'\right]}$$

$$\times \cosh y_{\mathrm{CM}} \left(\cosh\eta' - \tanh y_{\mathrm{CM}}\sinh\eta' \frac{p_{\perp}\cosh\eta'}{\sqrt{m^2+p_{\perp}^2\cosh^2\eta'}}\right). \quad (8.16)$$

A simple test of this not-so-simple expression is its normalization, which is easily (numerically) verified by integrating over η' at given m and β, for various values of y_{CM}.

This distribution is shown in Fig. 8.3, which parallels Fig. 8.2 with the same conventions and parameters. On comparing Figs. 8.2 and 8.3, we see that the rapidity and pseudorapidity spectra agree exactly for massless particles, since the pseudorapidity is the rapidity, in this case. The nearly massless pions are visibly little changed in spectral shape. With progressively increasing mass, the pseudorapidity spectra differ more from the rapidity spectra and, in particular, their center shifts to higher pseudorapidity.

There is a notable deformation of the symmetric shape accompanied by considerable widening – the peak is only 60% of the height of the original rapidity spectrum for $p_{\perp}^{\mathrm{min}} = 0$. In practical situations, the small-$p_{\perp}$ particles are eliminated, which we allow for by means of a cutoff in $p_{\perp}^{\mathrm{min}}$. We see that now the spectral shapes appear progressively less shifted from their rapidity form; the pseudorapidity and rapidity shapes become more similar, although a residual shift remains for the heaviest particles (nucleons). Thus the pseudorapidity–rapidity difference is primarily a low-momentum phenomenon. As the $p_{\perp}$ cutoff increases, the relative strength of the particle spectra changes and, in particular, there is considerable relative enrichment of the contributions of the heaviest particles compared with those of light particles.

8.2 A dynamic fireball

Naturally, a fireball at rest is not what we are likely to encounter in the highly dynamic situation of colliding nuclei. We now look at the modifications introduced by the presence of a local flow of matter. As before a volume element in a fireball is the particle source, but now this volume is in motion, typically due to a local flow originating from a (hydrodynamic)
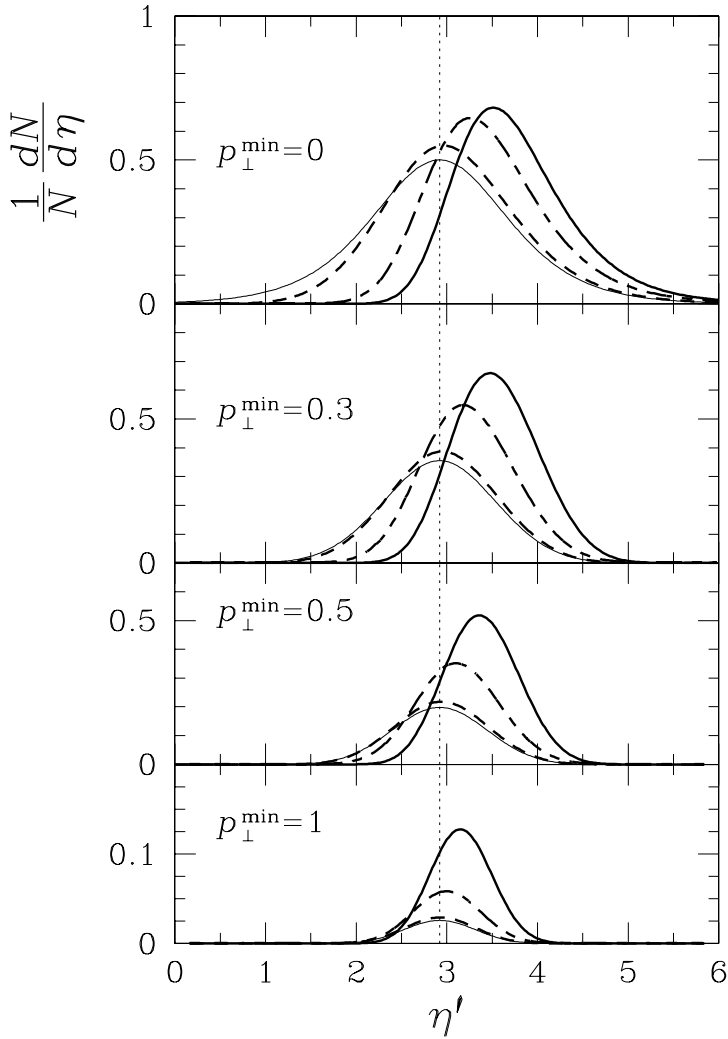
Fig. 8.3.   Particle spectra as a function of laboratory pseudorapidity η', for $\beta^{-1} = 160$ MeV, $y_{\mathrm{CM}} = 2.92$; massless particles (thin lines), π (dashed lines), K (chain lines), and N (solid lines). Results for various minimum transverse-momentum cutoffs are shown: $p_\perp^{\mathrm{min}} > 0$, > 0.3, > 0.5, and > 1 GeV. Note the change of scale for the last (bottom) case.

expansion. We will refer to this collective flow velocity below simply as $\vec{v}$. We would like to know how the statistical distribution appears to a laboratory observer. However, when we refer to a statistical phase-space distribution, we always imply an observer at rest in the local 'intrinsic' frame of reference. The 'intrinsic i' particle energy E^i and momentum

$\vec{p}^{\,i}$ are measured in the local non-flowing frame of reference of a moving volume element of the fireball.

We determine now how the intrinsic thermal spectrum appears to an arbitrary Lorentz observer, such as a laboratory observer is. The physical idea is to express the intrinsic thermal phase space in terms of Lorentz co-variant quantities, and than to use variables associated with any observer, e.g., a laboratory-frame observer. There are several approaches possible, and we proceed in the first instance to consider as in section 12.3 the Touschek invariant phase-space measure [143, 261]:

$$\frac{V_0 \, d^3 p^i}{(2\pi)^3} e^{-E^i/T} \rightarrow \frac{V_\mu p^\mu}{(2\pi)^3} \, d^4 p \, 2\delta_0(p^2 - m^2) e^{-p_\mu u^\mu/T}. \tag{8.17}$$

The flowing volume element $V_\mu = V_0 u_\mu$ is as observed in the laboratory frame. V_0 is the comoving volume element in the local rest frame. δ_0 is the Dirac delta function for the positive (energy) roots only, . It is an invariant function for all proper Lorentz transformations. The left-hand side of Eq. (8.17), is written in terms of the intrinsic variables, but the right-hand side is not frame-dependent and we can read it in the frame of reference of the laboratory observer.

We see the invariant measure introduced in Eq. (8.3):

$$2\delta_0(p^2 - m^2) \, d^4 p = \frac{d^3 p}{E} = m_\perp \, dm_\perp \, dy \, d\phi_p = p_\perp \, dp_\perp \, dy \, d\phi_p. \tag{8.18}$$

The particle momentum defined with reference to the collision axis has the explicit form

$$p^\mu = (m_\perp \cosh y, \, p_\perp \cos \phi^p, \, p_\perp \sin \phi^p, \, m_\perp \sinh y), \tag{8.19}$$

(in cylindrical coordinates) where we omit superscript p for the variables y and $m_\perp = \sqrt{m^2 + p_\perp^2}$, which, as usual, are understood to refer to the observed particle. We recall the usual relations,

$$\frac{m_\perp}{m} = \gamma_\perp = \cosh y_\perp, \quad \frac{p_\perp}{m} = v_\perp \gamma_\perp = \sinh y_\perp,$$

which allow us to write Eq. (8.19) in the form

$$\frac{p^\mu}{m} = (\cosh y_\perp \cosh y, \, \sinh y_\perp \cos \phi^p, \, \sinh y_\perp \sin \phi^p, \, \cosh y_\perp \sinh y).$$

This suggests that we introduce such a cylindrical representation of the velocity field as well,

$$u^\mu = (\cosh y_\perp^v \cosh y_\parallel^v, \sinh y_\perp^v \cos \phi^v, \sinh y_\perp^v \sin \phi^v, \cosh y_\perp^v \sinh y_\parallel^v),$$
$$u^2 = 1. \tag{8.20}$$

It is straightforward, in these coordinates, to obtain $u_\mu p^\mu$ required to construct the spectra in Eq. (8.17),

$$u_\mu p^\mu = \gamma_\perp^v \left[m_\perp \cosh(y - y_\parallel^v) - p_\perp v_\perp \cos\phi \right], \tag{8.21}$$

where $\gamma_\perp^v = \cosh y_\perp^v = 1/\sqrt{1 - v_\perp^2}$, $\phi = \phi^p - \phi^v$, and the variables y, $m_\perp$, and $p_\perp$ refer to the rapidity, the transverse momentum, and the transverse mass of the observed particle.

The explicit form of the invariant spectrum which generalizes Eq. (8.5), is

$$\boxed{\begin{aligned} \frac{d^2N}{m_\perp^2\, dm_\perp\, dy} &= \int \frac{d\phi\, \gamma_\perp^v}{(2\pi)^3} \left(\cosh(y - y_\parallel) - \frac{p_\perp}{m_\perp} v_\perp \cos\phi \right) \\ &\times \exp\left\{ -\gamma_\perp^v \left[m_\perp \cosh(y - y_\parallel) - p_\perp v_\perp \cos\phi \right]/T \right\}. \end{aligned}} \tag{8.22}$$

For a suitable choice of the coordinate system in which the x axis is pointing in the direction of the transverse flow vector, $\phi^v = 0$, the particle-emission angle is the azimuthal angle of integration $\phi = \phi^p$. We use the range $0 < \phi \le \pi$, which has to be counted twice to include the part $\pi < \phi \le 2\pi$. The ϕ integrals we encounter are analytical:

$$\frac{1}{\pi} \int_0^\pi e^{\pm a \cos\phi}\, d\phi = I_0(a), \quad \frac{1}{\pi} \int_0^\pi e^{\pm a \cos\phi} \cos\phi\, d\phi = \pm I_1(a). \tag{8.23}$$

It is helpful to remember that I_0 'looks like' a cosh function, and I_1 like a sinh function, and the analogy goes further with

$$I_1(a) = \frac{\partial I_0(a)}{\partial a}. \tag{8.24}$$

However,

$$\cosh a = I_0(a) + 2I_2(a) + 2I_4(a) + 2I_6(a) + \cdots, \tag{8.25}$$
$$\sinh a = 2I_1(a) + 2I_3(a) + 2I_5(a) + \cdots, \tag{8.26}$$

where

$$\boxed{I_n(a) = \frac{1}{\pi} \int_0^\pi e^{a \cos\phi} \cos n\phi\, d\phi = \sum_{k=0}^\infty \frac{(a/2)^{2k+n}}{k!(n+k)!}.} \tag{8.27}$$

Using Eq. (8.23) in Eq. (8.22), we obtain

$$\frac{d^2 N}{m_\perp^2 \, dm_\perp \, dy} = \frac{\gamma_\perp^v}{(2\pi)^2} \left(\cosh(y - y_\parallel) \, I_0(p_\perp v_\perp / T) - \frac{p_\perp}{m_\perp} v_\perp I_1(p_\perp v_\perp / T) \right)$$
$$\times \exp\left[-\gamma_\perp^v m_\perp \cosh(y - y_\parallel)/T \right]. \tag{8.28}$$

This is the statistical particle spectrum seen in the laboratory frame and originating in a volume element of a fireball having two velocity components $y_\parallel$ and $v_\perp$, and emitting particles at the local temperature T. If the laboratory frame is not the CM frame, we need to shift the rapidity $y \to y - y_{\mathrm{CM}}$. This is the particle spectrum of final-state hadrons arising if the matter in the entire volume of the fireball froze out suddenly.

This volume-style statistical phase-space hadronization based on work carried out by Touschek [261], differs from the approach of Cooper and Frye [96], which allows for the dynamics of the particle-emitting surface. One imagines an opaque fireball, and each surface element is the particle source. The physical idea is thus to couple the intrinsic (statistical) particle spectrum to the Lorentz-covariant surface dynamics. The developments till 1993 are well documented in [238]. It was subsequently discovered that the radiation formula was non-positive definite and a generalization was proposed [119].

The particle phase space is written using a covariant surface in $4 - 1 = 3$ space–time dimensions. Consequently, apart from the flow, there is yet another velocity that describes how the hadronization surface moves, e.g., the surface may be flowing outward, but a rapid 'peeling' of matter may move the boundary of the particle-producing volume inward. Moreover, over the history of the particle production (freeze-out from the surface), the surface may have both positive and negative velocities, and thus it can be difficult to make sure that a particle is actually emitted rather than absorbed in the fireball.

We now illustrate the difficulty inherent in dealing with the problem of emission of particles, which continues to be actively studied. First, we recall how, in the Touschek approach, the particle density in phase space has been written in a Lorentz-invariant way as

$$\frac{d^6 N}{d^3 x \, d^3 p} = \frac{g}{(2\pi)^3} e^{-u_\mu p_i^\mu / T}, \tag{8.29}$$

where u^μ is the 4-flow velocity. In the volume-hadronization approach, we have made the following qualitative steps:

$$E \frac{d^3 N}{d^3 p} = \frac{dN}{d\phi \, dy \, m_\perp \, dm_\perp}$$
$$= \frac{g}{(2\pi)^3} e^{-u_\mu p_i^\mu / T} \left[E_i \, d^3 x \to p_i^\mu V_\mu \propto p_i^\mu u_\mu \right]. \tag{8.30}$$

When surface emission dominates the particle spectra, the other way to proceed is

$$E\frac{d^3N}{d^3p} = \frac{g}{(2\pi)^3}e^{-u_\mu p_i^\mu/T}\left[E_i\,d^3x \rightarrow \right.$$
$$\left. \int d\tau\,d^3\Sigma_f^\mu p_{\mu\,i}\,\delta\left(d\tau - \sqrt{dt_f^2 - d\vec{x}_f^2}\right)\right], \quad (8.31)$$

where $x_f^\mu = (t_f, \vec{x}_f)$ are the freeze-out surface coordinates, and Σ_f^μ is the three-dimensional hypersurface of the Minkowski volume element, characterized by a unit 4-vector normal to the surface u_f^μ, i.e., the 4-velocity of the freeze-out surface:

$$n_s^\mu = \frac{dx_f^\mu}{d\tau} = \frac{dt_f}{d\tau}\left(1, \frac{d\vec{x}_f}{dt_f}\right). \quad (8.32)$$

Equation (8.31) arises since we wish to sum the emission spectrum over the contributions made by each surface element $d^3\Sigma$ over its (proper time τ) history. For a fireball at rest, we have $n_f^\mu = (1, 0, 0, 0)$, $d^3\Sigma_f^\mu = dt_f\,d^2x_f$, and $\vec{v}_f = d\vec{x}_f/dt_f = 0$. Noting that the δ-function simply sets the proper time to the freeze-out time, we obtain

$$E\frac{d^3N}{d^3p} = \frac{g}{(2\pi)^3}\,e^{-E_i/T}E_iS_f\,\Delta t_f, \quad (8.33)$$

where Δt_f is the length of (proper) time during which the emission of particles occurs, and S_f is the size of the surface.

For simple geometries, we can use

$$d\tau\,\delta\left(d\tau - dt_f\sqrt{1 - d\vec{x}_f^2/dt_f^2}\right) = \delta\left(1 - \frac{dt_f}{d\tau}\sqrt{1 - d\vec{x}_f^2/dt_f^2}\right) \rightarrow 1,$$

and we find the conventional Cooper–Frye formula:

$$E\frac{d^3N}{d^3p} = \frac{dN}{d\phi\,dy\,m_\perp\,dm_\perp} = \frac{g}{(2\pi)^3}\int_{\Sigma_f}e^{-E^i/T}\,p_\mu^i\,d^3\Sigma^\mu. \quad (8.34)$$

$d^3\Sigma^\mu$ is the normal surface vector for the four-dimensional space–time volume boundary, from which the emission of particles occurs,

$$d^3\Sigma^\mu \equiv \epsilon_{\mu\nu\lambda\rho}\frac{\partial\Sigma^\nu}{\partial u}\frac{\partial\Sigma^\lambda}{\partial v}\frac{\partial\Sigma^\rho}{\partial w}\,du\,dv\,dw, \quad (8.35)$$

where u, v, w is a suitable set of three locally orthogonal coordinates. In cylindrical coordinates $(u, v, w) = (r_f, \phi_f, z_f)$ and

$$\Sigma_f^\mu = (t_f, r_f\cos\phi_f, r_f\sin\phi_f, z_f). \quad (8.36)$$

The freeze-out time t_f is independent of the angle ϕ_f due to the assumption of cylindrical symmetry and thus we have $t_f(r_f, z_f)$. The covariant volume element is

$$d^3\Sigma_\mu^{cyl} = \left(1, -\frac{\partial t_f}{\partial r_f}\cos\phi_f, -\frac{\partial t_f}{\partial r_f}\sin\phi_f, -\frac{\partial t_f}{\partial z_f}\right) r_f\, dr_f\, d\phi_f\, dz_f. \quad (8.37)$$

We use the momentum vector of a particle p_i^μ in cylindrical coordinates, Eq. (8.19), and obtain

$$\frac{d\tau}{dt_f} p^\mu\, d^3\Sigma_\mu^{cyl} = r_f\, dr_f\, d\phi_f\, dz_f \left[m_\perp\left(\frac{1}{u_f^0}\cosh y - \frac{1}{u_f^\parallel}\sinh y\right)\right.$$
$$\left. -\frac{1}{u_f^\perp}p_\perp\cos\phi\right], \quad (8.38)$$

where as before $\phi = \phi^f - \phi^p$.

The 4-velocity of the freeze-out surface is

$$dx^\mu/d\tau = u_f^\mu = (u_f^0, u_f^\perp\cos\phi_f, u_f^\perp\sin\phi_f, u_f^\parallel).$$

This additional surface dynamics influences the observed spectra, even though we are dealing with a preexponential factor only. The transverse-mass spectra contain an additional factor, compared to Eq. (8.22),

$$\frac{d^2 N}{m_\perp\, dm_\perp\, dy} \rightarrow \int \frac{d\phi\, \gamma_\perp^v}{(2\pi)^3}\left(1 - \frac{\vec{v}_{fr}^{-1}\cdot\vec{p}}{E}\right)$$
$$\times\left(\cosh(y - y_\parallel) - \frac{p_\perp}{m_\perp}v_\perp\cos\phi\right) \quad (8.39)$$
$$\times\exp\left\{-\gamma_\perp^v\left[m_\perp\cosh(y - y_\parallel) - p_\perp v_\perp\cos\phi\right]/T\right\},$$

where

$$\vec{v}_{fr}^{-1}\cdot\vec{p} \equiv \frac{\partial t_f}{\partial r_f}p_\perp\cos\phi + \frac{\partial t_f}{\partial z_f}p_z. \quad (8.40)$$

Particles are emitted from the surface of fireball volume, and thus the phase space is $(2 + 2)$-dimensional when the number of particles is counted. For this dimensional reason there is one power of $m_\perp$ less in Eq. (8.39), than there is in Eq. (8.22). When $v_{fr} \rightarrow c$ the prefactor in Eq. (8.39) is able to compensate for this effect and both methods can describe the experimental hadron spectra with similar precision.

We proceed to show how the longitudinal flow, and, in section 8.4, the transverse flow, influence particle spectra. Numerical study shows that the two flows are practically independent from each other, and it has
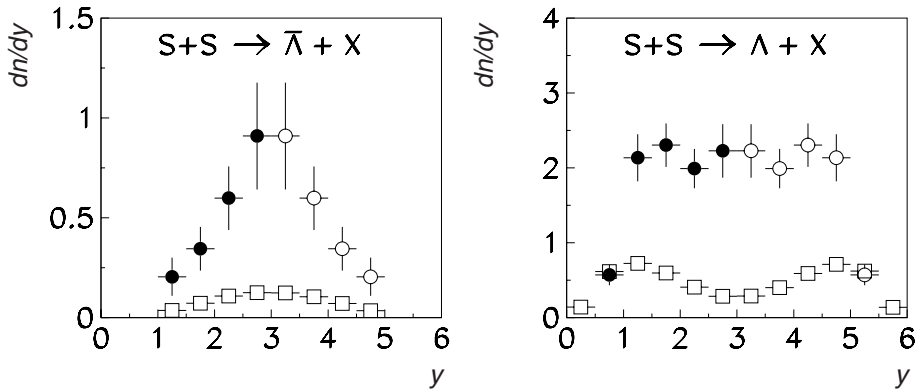
Fig. 8.4. On the left, the abundance of $\overline{\Lambda}$ in S–S collisions at $200A$ GeV, as a function of rapidity. The squares are the results for N–N collisions scaled up by the pion-multiplicity ratio. On the right, corresponding results for the abundance of Λ. Data produced by the NA35 collaboration [24].

become commonplace to study particle spectra as if either only parallel or only transverse flows were present: in a study of rapidity spectra, only $y_{\parallel}$ is considered, while $v_{\perp}$ is ignored; in a study of $m_{\perp}$ spectra, the longitudinal flow $y_{\parallel}$ is not considered.

8.3 Incomplete stopping

Considering that, at very high collision energies, the longitudinal scaling behavior is expected, see section 6.3, whereas in collisions of large nuclei at moderate energies a central fireball is more appropriate, it is natural that the real world is observed to be much more complex than these simple 'asymptotic' models.

A nice example of the case in which the baryon number just does not punch through is seen in the central $200A$-GeV S–S collisions at the SPS. We show, in Fig. 8.4, the production yields of $\overline{\Lambda}$ (left-hand side) and Λ (right-hand side) hyperons as functions of rapidity. The open circles in Fig. 8.4 are the directly measured data. The particle spectra must be symmetric around the CM rapidity, since this is a symmetric collision system. For this reason the open black circles are obtained by reflecting the measured data points (solid black circles) at the value $y = 2.96$.

The spectra arising from N–N interactions at the same energy are shown in Fig. 8.4 (open squares). These N–N-interaction comparison data have been multiplied by the rapidity-dependent pion-multiplicity-enhancement factor, which accounts for the increase in production of
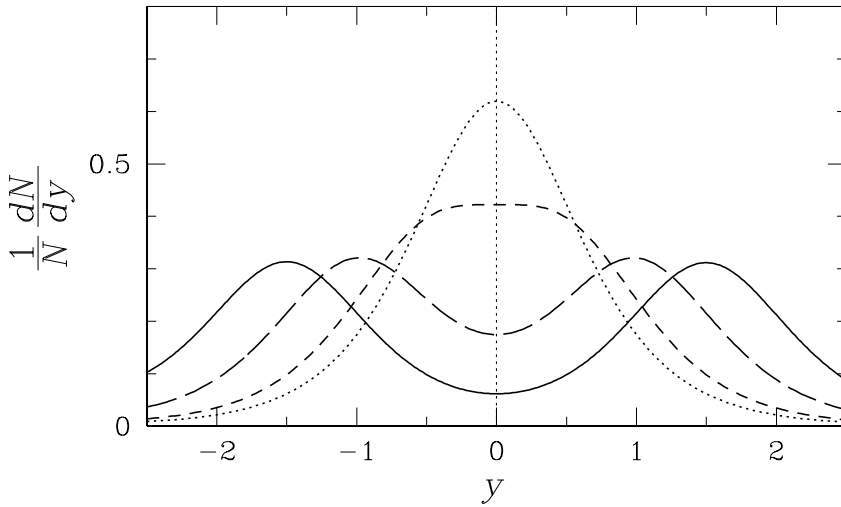
Fig. 8.5.   Rapidity spectra of massless QGP quanta with flow: dotted, no flow $y_\parallel = 0$; short-dashed, $y_\parallel = 0.5$; long-dashed $y_\parallel = 1$; and solid, $y_\parallel = 1.5$ [178].

pions per nucleon observed on comparing S–S with N–N reactions. In the target ($y = 0.75 \pm 0.25$) and projectile ($y = 5.25 \pm 0.25$) fragmentation regions, this procedure gives a good agreement between yields of Λ particles in S–S and N–N scaled by the pion multiplicity. This suggests that, in the target/projectile fragmentation regions, the production of Λ has the same origin in both cases, presumably from individual N–N interactions.

However, in the central rapidity region in Fig. 8.4, new mechanisms of production of $\overline{\Lambda}$ and Λ are clearly visible. Inspecting the yield of $\overline{\Lambda}$, we see considerable localization at central rapidity of a particle made entirely from constituents not brought into reaction, $\overline{\Lambda}(\overline{u}\overline{d}\overline{s})$. Naturally, there must have been associated localization of the energy. The Λ rapidity spectrum is, in contrast, relatively flat. $\Lambda(uds)$ contains, aside from the strange quark made in the reaction, constituent quarks brought into the collision region by the projectile and target. Were the punch through of the light (u, d) quark content complete, we should see for Λ a distribution similar to $\overline{\Lambda}$, both in shape and in yield.

We consider now the rapidity spectra in the presence of a longitudinal flow $y_\parallel$, evaluating the $m_\perp$ integral in Eq. (8.22). The challenge is to describe a diversity of rapidity spectra of observed hadrons, which are very strongly varying between certain particles. The different behaviors are shown schematically in Fig. 8.5. We see how the thermal rapidity spectra of massless quanta in the deconfined phase, with $m = 0$, (and with $T = 145$ MeV, and $v_\perp = 0.52$, which values matter little), vary.
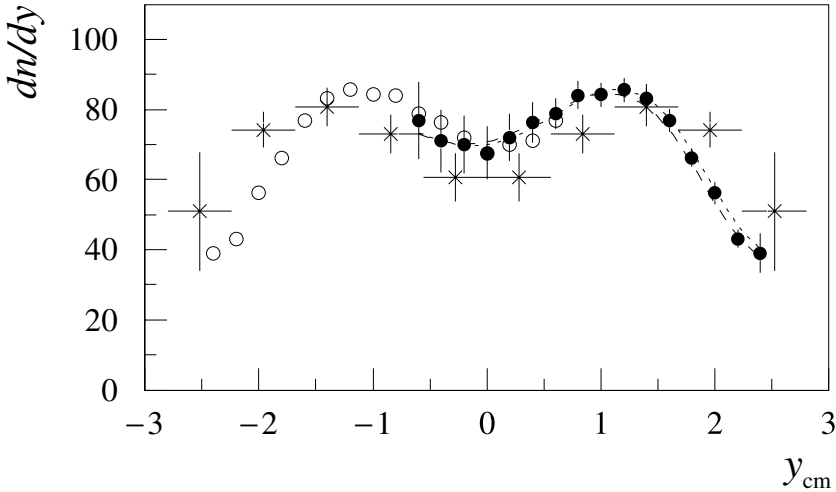
Fig. 8.6.   Rapidity spectra of baryons $\langle b - \bar{b} \rangle$ observed by experiment NA49 [43] in central (5%) Pb–Pb interactions at $\sqrt{s_{\mathrm{NN}}} = 17.2$ GeV (solid circles, direct measurement; open circles, reflection at y_{CM}). Stars are rapidity spectra of baryons for S–S interactions obtained by NA35 at $\sqrt{s_{\mathrm{NN}}} = 18.4$ GeV, for the 3% most central events, scaled with participant number 352/52.

These gradually 'flow' apart as $y_\parallel$ is increased from $y_\parallel = 0$ (dotted line) to $y_\parallel = 1.5$ (solid line) in steps of 0.5.

Comparing with Fig. 8.4, we see that both limits (the central production of $\overline{\Lambda}$ and the flat distribution of Λ) are seen in Fig. 8.5. How can this be happening in the same reaction? In order to obtain different types of flow for different particles, we presume in the following illustrative example that hadrons arise from a mix of three quark fluids. The incoming valence quarks of colliding nuclei are retaining some ($v_\parallel^{\mathrm{valence}} \neq 0$) memory of the original motion along the collision axis, and constitute the projectile and target fluids. However, all newly made pairs of quarks have practically no memory ($v_\parallel^{\mathrm{pair}} \simeq 0$) of the initial condition of colliding matter, they are formed near y_{CM} and are constituents of the third fluid. In particular, pairs of strange quarks made in the plasma do not flow in the longitudinal direction.

For the protons produced, this model implies that all three quarks remember the incoming flow and their distribution should follow the solid or long-dashed line (depending on $y_\parallel$). For Λ, with one strange quark, we consider a mix of two thirds weight in the spectrum with flow and one thirds without. For particles like $\mathrm{K}^+(\mathrm{u}\bar{\mathrm{s}})$, we take a 50%–50% mix, and, for all newly made particles like $\overline{\Lambda}$ and Φ, we assume that only no-flow components contribute. To describe baryon rapidity spectra in Pb–Pb
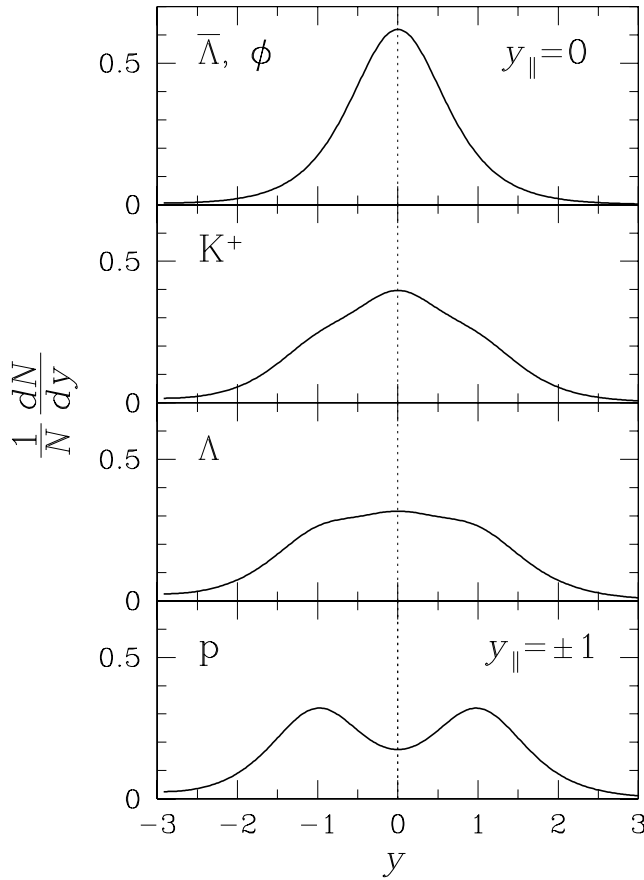
Fig. 8.7. Schematic representations of rapidity particle spectra within a thermal model with flow, parameters chosen for $\sqrt{s_{\mathrm{NN}}} = 17.2$ GeV [178].

collisions at $\sqrt{s_{\mathrm{NN}}} = 17.2$ GeV, reported by NA49 [43], see Fig. 8.6, we assume that the longitudinal flow is $y_\parallel \simeq \pm 1$, and choose this value without attempting to fit the spectra.

The proton rapidity spectrum is shown in the bottom panel in Fig. 8.7. We used $m_{\mathrm{q}} = 0$, $T = 145$ MeV, and $v_\perp = 0.52c$, which parameters hardly matter and could be chosen very differently; these values were taken in view of the $m_\perp$ spectra we discuss below in section 8.4. We average over positive and negative flows $y_\parallel = \pm 1$, since the collision in the CM frame involves both. The strange-quark content of the Λ which contributes with relative strength 33% suffices to yield a flat distribution – see the second panel from the bottom in Fig. 8.7. The shape of the central rapidity plateau is in agreement with the results seen in NA49 data, as well as with those shown above in Fig. 8.4 for the NA35 S–S collisions.

In the third panel from the bottom, corresponding to the 50%–50% flow mix such as would be appropriate for $K^+(u\bar{s})$, the resulting rapidity shape is already peaked at the central rapidity. Finally, in the top panel, we show a prototype of the rapidity distribution arising for all hadrons made from completely newly made particles such as $\overline{\Lambda}$ and Φ. The measured Φ spectrum is again in qualitative agreement with this result [21].

A comparison of the baryon distributions between Pb–Pb and S–S collision, seen in Fig. 8.6, suggests that $y_\parallel$ is about 0.4 units of rapidity larger in the lighter collision system. Even though it is seemingly a small change, this opens by 50% the gap between the fluids, as we saw in Fig. 8.5, and a more pronounced central-rapidity reduction in abundances of certain particles is present for S–S compared with Pb–Pb collision systems.

8.4 Transverse-mass fireball spectra

The experimental study of the rapidity spectra is complemented by studies of particle-abundance distributions in the direction transverse to the collision axis. Under a Lorentz transformation along the collision axis, $p_\perp$ remains unchanged and thus

$$m_\perp = \sqrt{m^2 + \vec{p}_\perp^2}$$

is invariant. Transverse-mass $m_\perp$-particle spectra are therefore not directly distorted by flow motion of the fireball matter along the collision axis, and also no further consideration of the CM frame of reference is necessary, which in fixed target experiments is rapidly moving with respect to a laboratory observer.

There is also a great difference in the physics when we evaluate rapidity and transverse-mass spectra. As discussed in section 8.3, the rapidity spectra help us understand the degree of stopping and transparency of matter in collision, whereas the $m_\perp$ spectra offer insights into thermalization of matter after collision, and evolution of flow. In that sense $m_\perp$ spectra are often more interesting and also a greater challenge to describe in an *ab initio* study. Within the statistical model the focus in studying $m_\perp$ spectra is on determining the local temperature and transverse flow of the evolving fireball matter.

One could consider the particle spectra as functions of transverse-momentum $p_\perp$, but the regularities occurring for transverse-mass spectra for different particles suggest that the spectra have a thermal character. Therefore $m_\perp$ is a better variable to use in heavy-ion collisions, at least when $m_\perp$ is not too big: particles with high values of $m_\perp > 4$ GeV, at the temperatures we consider, are potentially produced in initial hard scattering of partons. These decay in yield as a power law, and hence

dominate the exponentially decaying thermal particle yields at high $m_\perp$. Since hard parton scattering knows nothing about the mass of the final hadron observed, a better variable to look at to evaluate these processes is $p_\perp$. However, for $m_\perp \gg m$, there is little difference between $p_\perp$ and $m_\perp$, so we conclude that $m_\perp$ is overall the more suitable variable to consider in heavy-ion collisions. One of the surprising early results obtained at RHIC is the absence of high-$p_\perp$ particles in central interactions [17]. This suggests an effective parton thermalization mechanism.

In order to study the thermal properties in the fireball as 'reported' by the emitted particles, we analyze $m_\perp$ spectra of many different hadrons. The range of $m_\perp$, on the one hand, should not reach very large values, at which hadrons originating in hard parton scattering are relevant. On the other hand, we do need relatively small $m_\perp$, in order for the non-exponential structure associated with transverse flow and resonance decays to emerge.

The transverse-mass spectra of hyperons, which we have seen in Fig. 1.7 on page 20, are potentially very important in understanding and in modeling of the exploding QGP fireball. We have already in the S–Au $200A$-GeV collisions the appearance of the exponential thermal spectra. The central-rapidity high-transverse-mass spectra of strange particles, K_s^0, $\overline{\Lambda}$, and Λ, given by the CERN–SPS WA85 collaboration, $m_\perp^{-3/2} dN_i/dm_\perp$, are shown in Fig. 8.8. The factor $m_\perp^{-3/2}$ is introduced in view of the form of Eq. (8.8). The resulting shape, shown in Fig. 8.8 on a semi-logarithmic display, can be fitted with a straight line. This exactly exponential behavior is initially surprising, considering that Eq. (8.8) required summation over the entire range of rapidity, given the rapidity acceptance range of WA85 limited to central $\Delta y < 1$ interval. However, effective summation over a wider range of y occurs, given the presence of collective longitudinal flow of matter. Similar results were also reported from the related work of the WA94 collaboration for S–S interactions [8].

We see, in Fig. 8.8, in the region of transverse masses presented, 1.5 GeV $< m_\perp <$ 2.6 GeV, not only that the particle spectra are exponential, $\propto \exp(-m_\perp/T_\perp)$, but also that the behaviors of all three different particles feature the same inverse slope, $T_\perp = 232 \pm 5$ MeV. This is not the actual temperature of the fireball, as noted earlier. The lower emission temperature of these particles, T_{tf}, is blue-shifted by the flow as is seen in Eq. (8.39), and can be approximately understood in terms of the Doppler factor in Eq. (5.36).

The same shape of $m_\perp$ spectrum appears in results from the WA80 collaboration results, for the neutral hadrons π^0 and η. In Fig. 8.9, we show the S–Au and S–S WA80 results at $200A$ GeV [28, 29, 234, 235], multiplying the invariant cross sections by the power $m_\perp^{-1/2}$ in order to establish
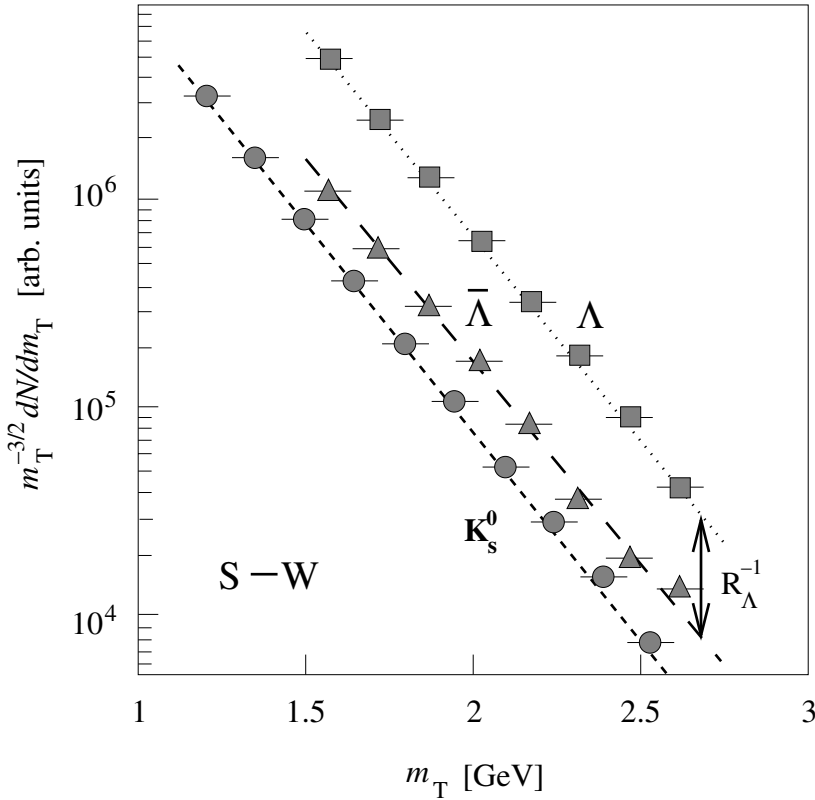
Fig. 8.8.   Strange-particle spectra for Λ, $\overline{\Lambda}$, and K_S [225]. The line connecting the Λ and $\overline{\Lambda}$ spectra, denoted R_Λ^{-1}, shows how at fixed $m_\perp$ the ratio R_Λ of abundances of these particles can be extracted. Experimental WA85 results at $200A$ GeV [104, 116, 117].

a direct correspondence between the representations of the data of experiments WA85 and WA80. To determine the required multiplicative factor, we note that the particle-production cross section $d\sigma$ is controlled by the geometry of the collision, see section 5.2, and thus is the geometric interaction surface, σ_{inel}, multiplied by the yield of particles dN. Using Eq. (8.3) we obtain

$$m_\perp^{-1/2} E \frac{d^3\sigma}{d^3p} = \sigma_{\text{inel}} \frac{dN}{2\pi\, m_\perp^{3/2}\, dm_\perp\, dy}. \tag{8.41}$$

Like WA85, the WA80 experiment also presented data for the central region in rapidity, $2.1 < y < 2.9$, and no further adjustment is needed in order to make the results exactly comparable.
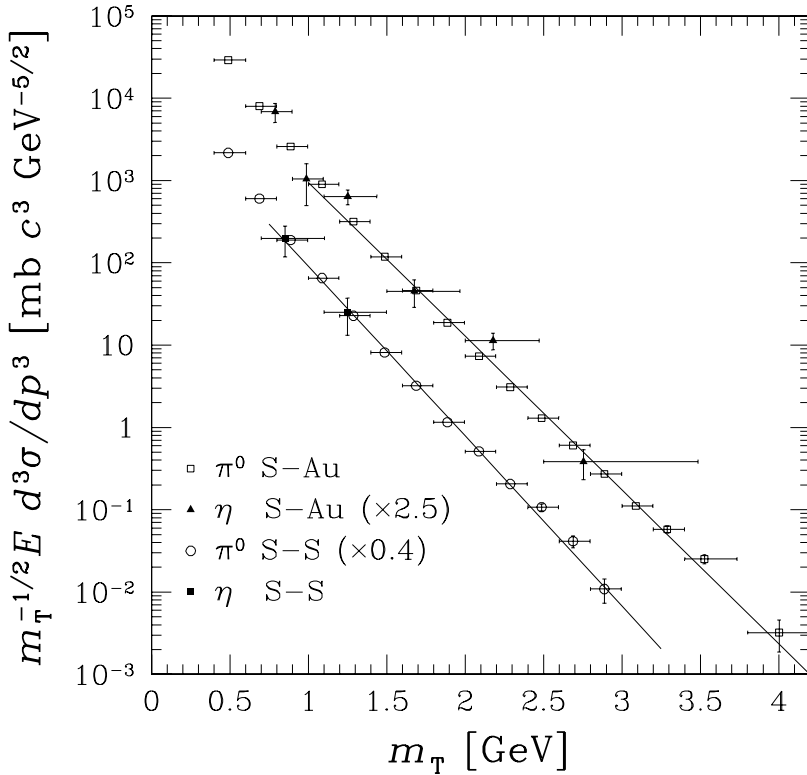
Fig. 8.9. Neutral-particle π^0 and η spectra (invariant cross sections divided by $m_\perp^{1/2}$) in the central-rapidity interval $2.1 < y < 2.9$ [225]. Upper solid line, S–Au thermal spectrum with temperature $T = 232$ MeV; lower solid line, S–S, $T = 210$ MeV. Experimental data at $200A$ GeV courtesy of the WA80 collaboration [28, 29, 234, 235].

The upper straight line (S–Au collisions) in Fig. 8.9 is the same exponential as we saw in Fig. 8.8, for the three different WA85 strange-particle spectra. While the WA85 data covered the interval 1.5 GeV $< m_\perp < 2.5$ GeV, the thermal exponential shape continues, in the WA80 data, through the highest data point at $m_\perp = 4$ GeV. The lower solid line in Fig. 8.9 is for S–S $200A$-GeV interactions and is drawn with $T = 210$ MeV. The choice of S–S temperature is based on the WA94 results obtained from their spectra of strange antibaryons [8]. It is noteworthy that the WA80 particle spectra shown in Fig. 8.9 span seven decades, and that over 5–6 decades the thermal spectral shape for neutral hadrons is in excellent agreement with the strange-particle spectral shape. We note that the rise in the yield of neutral mesons at low $m_\perp \simeq 0.5$ GeV is expected. It is due to secondary contributions to the yield of particles by decay of hadronic

Table 8.1. Inverse (net) proton slopes $T_\perp$ for various reaction systems at $200A$ GeV ($158A$ GeV for Pb–Pb), increasing in size from left to right

Reaction	p–S	p–Au	d–Au	O–Au
$T_\perp$	154 ± 114	163 ± 5	172 ± 5	219 ± 5
y interval	$0.5 \le y \le 3.0$	$0.5 \le y \le 3.0$	$0.5 \le y \le 3.0$	$0.5 \le y \le 3.0$
Reaction	S–S	S–Ag	S–Au	Pb–Pb
$T_\perp$	235 ± 9	238 ± 2	276 ± 48	308 ± 15
y interval	$0.5 \le y \le 3.0$	$0.5 \le y \le 3.0$	$3.0 \le y \le 5.0$	$y \simeq 3$

resonances. While at high $m_\perp$ pion, kaon, and hyperon slopes agree, at small $m_\perp < 0.8$ GeV the pion spectrum is much steeper. Since most pions are produced at these $m_\perp$, a global fit to the pion data yields an inverse slope parameter which is much smaller than the value we can see in Fig. 8.9.

There is a clear difference between $T_\perp$ inverse slopes pertinent to different collision systems, and a systematic trend is visible: $T_\perp$ increases with the volume of the reaction zone. We show, in table 8.1, the $m_\perp$ inverse slopes of participating (net) protons for a number of collision systems studied by the NA35/NA49 collaboration [26, 43]. The shape of the $m_\perp$ spectra has been fitted to the simple form

$$\frac{dN}{dm_\perp\, dy} \sim m_\perp^\alpha \exp(-m_\perp/T). \tag{8.42}$$

The results presented in table 8.1 were obtained with $\alpha = 1$. Several effects contribute to an increase of $T_\perp$ with increasing size of the colliding system. With increasing number of participants in the collision, the fireball of dense matter becomes less transparent and thus colliding matter can be compressed more at a given collision energy. Moreover, larger systems have more time to develop the outward flow under the (higher) internal pressure, acquiring a greater collective velocity. Thus, what we see is that the initial fireball of the collision system is getting hotter and denser with increasing collision volume, which leads to a longer, and more violent explosion. This in turn enhances the transverse velocity at the time of production of particles. An in-depth analysis, which requires consideration of other particles apart from the (net) production of protons, confirms that the systematic increase of the inverse $m_\perp$ slope with increasing size of the system is associated with an increasing velocity of expansion of the source. The intrinsic temperature of emission from the fireball remains at the level of $T \lesssim 160$ MeV [59, 60, 176, 259].

Table 8.2.   Inverse slopes $T_\perp$ for various strange hadrons

	Λ	$\overline{\Lambda}$	Ξ^-	$\overline{\Xi}^+$	$\Omega^- + \overline{\Omega}^+$	ϕ
Pb–Pb	289 ± 2	287 ± 4	286 ± 9	284 ± 17	251 ± 19	305 ± 15
S–W	233 ± 3	232 ± 7	244 ± 12	238 ± 16		

To reach the most extreme conditions, collisions of the heaviest nuclei are required, and thus much of the experimental effort has gone into studying the Pb–Pb collision system. The highest inverse slopes are reported for several strange baryons and antibaryons by the WA97 collaboration [42]. Results presented in table 8.2 were obtained using, in Eq. (8.42), $\alpha = 1$ for Pb–Pb, and $\alpha = \frac{3}{2}$ for the S–W collision system. The corresponding spectra are shown in Fig. 1.7 on page 20. The most interesting result seen in table 8.2 is that there is practically the same inverse slope for baryons and antibaryons of the same type. This confirms the result reported by the WA85 collaboration for S–W interactions [6, 118], as is also shown in table 8.2.

The data point in table 8.2 for the $\phi(s\bar{s})$, in Pb–Pb collisions, is from the evaluation of the kaon-decay channel by the NA49 collaboration [21]. This data point disagrees with a preliminary result $T_{\mu\mu} = 227$ MeV, which was reported by the NA50 collaboration and obtained in the dimuon-decay channel [212].

If strange baryons and antibaryons were to be produced in an environment of baryon-rich confined matter, the difference in interactions of antibaryons, which have a large annihilation cross section at small momenta, should be visible as a baryon–antibaryon difference in the spectral shape, in particular at small $m_\perp$. The absence, to a very high precision, of any transverse-mass spectral asymmetry between strange baryons and antibaryons is a very important item of experimental evidence for a common mechanism of production of strange baryons and antibaryons by a source such as a QGP fireball which treats matter and antimatter in the same way. In order to suppress interactions within a hadronic-matter phase possibly formed after the QGP state hadronizes, either a sudden breakup of the fireball, arising after considerable super-cooling, or sequential evaporation of hadrons in time, without formation of a hadron phase, is required. This symmetry between matter and antimatter has not been reproduced in transport models, in which confined hadron degrees of freedom appear.

In Fig. 8.10, we see, for Pb–Pb collisions at $158A$ GeV, results shown in table 8.2 along with other inverse slopes $T_\perp$ ordered as functions of particle mass. Several different results are shown for pions, which arise
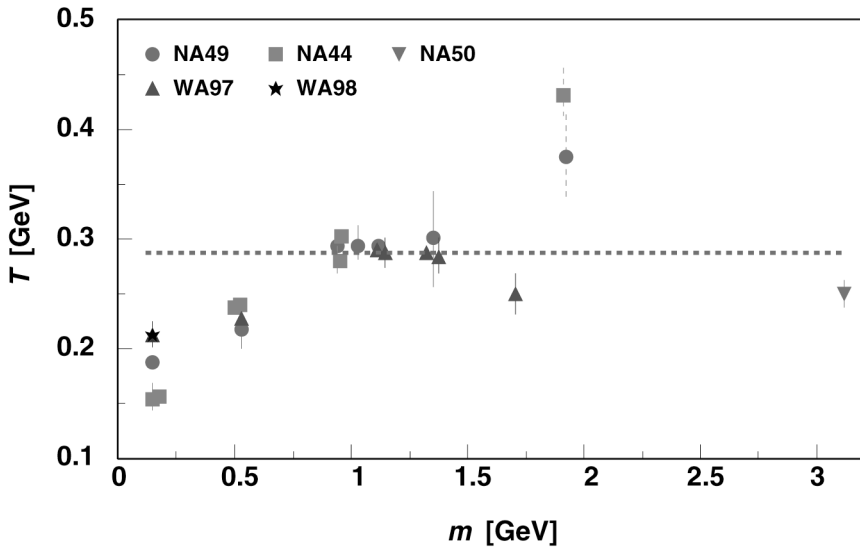
Fig. 8.10. Mass dependences of inverse slopes observed in Pb–Pb interactions at $158A$ GeV; symbols indicate the experiment from which data is drawn, as coded in the figure.

for different (low) $m_\perp$, y windows considered in different experiments. Even so, there is some unresolved variance between different pion results. Ten different hadronic particles with 0.9 GeV $< m <$ 1.5 GeV exhibit a common inverse slope indicated by the horizontal dashed line. There is general agreement that the increase in the slope seen on comparing pions, kaons, and baryons (obtained within an overlapping range of $p_\perp$, not of $m_\perp$) is due to the presence of a strong transverse flow of matter from which these particles originate [59]. The observation of a thermal charmonium spectrum (the point at $m = 3.1$ GeV) both in S- and Pb-induced reactions [11, 14], with $m_\perp$ slopes similar to those for the other heavy hadrons, suggests that thermalization of hadrons is a universal phenomenon in heavy-ion collisions. The thermal shape of the observed charmonium spectra is somewhat surprising considering the 'standard-model' reaction picture of suppression of charmonium, see section 1.6.

The highest value of T in Fig. 8.10, at $m = 1.9$ GeV, for the deuteron, confirms that these particles are not produced thermally. Production of deuterons is believed to arise predominantly from the final-state interaction between nearly free-streaming nucleons. The inverse slope for Ω and $\overline{\Omega}$ (at $m = 1.6$ GeV) seems to be about two standard deviations below expectation. It is understood to be due to excess production of Ω and $\overline{\Omega}$ at low $p_\perp$; see Fig. 8.11.
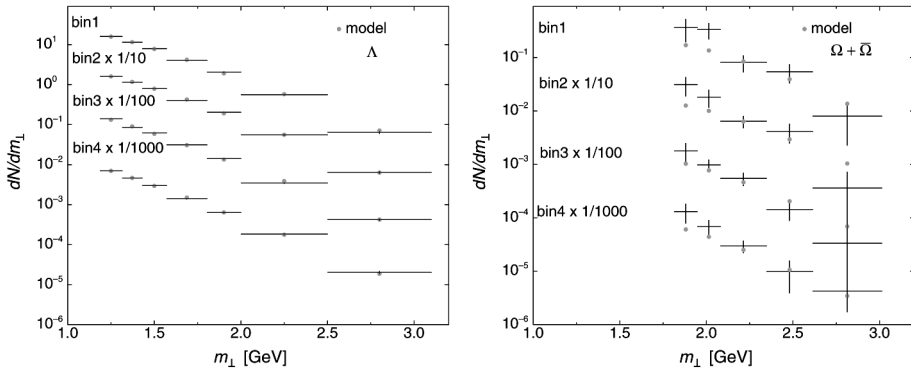
Fig. 8.11.   Thermal analysis of Λ (left) and $\Omega+\overline{\Omega}$ (right) $m_\perp$ spectra for various centralities of collision [259].

8.5 Centrality dependence of $m_\perp$-spectra

A study of transverse-mass spectra [259] has been performed for the precisely known strange-hadron spectra of the experiment WA97 [42], reported for several centrality bins; this data, with all centrality bins combined, is shown in Fig. 1.7 on page 20. The shapes of the various particle spectra depend in a complex, nonlinear, but unique, way, on the temperature used, and on the velocity of transverse flow, and these parameters are determined universally for all particles considered in each collision centrality.

In an early study of hadron spectra it was suggested that spectra alone could not separate $T_{\rm tf}$ and $v_{\rm tf}$, as these quantities are highly correlated; see the Doppler formula Eq. (5.36). As we will see, these two parameters can be determined without any need for other experimental input, when precise experimental data are available for $m_\perp$ spectra reaching down to relatively low values of $p_\perp$. This is possible for the following reason: it is assumed that, after hadronic resonances have decayed, their decay products do not rescatter from surrounding matter, thus the non-thermal spectrum is combined with the primary thermal spectrum to form the final observed spectrum. By choosing the yield of resonances to be determined by the temperature seen in the spectrum, the shape of the computed spectrum becomes a highly nonlinear function of temperature and velocity. Since there is a minimum transverse momentum required in order to observe a particle, the yields above $p_\perp^{\rm min}$ depend also on the transverse-flow velocity. This method assumes that the chemical (particle-production) freeze-out temperature $T_{\rm f}$ is assumed to be nearly equal to the thermal (spectrum-shaping) freeze-out temperature $T_{\rm tf}$. The results obtained are consistent with this assumption.

The final $m_\perp$ distribution for particles is composed of directly produced particles and decay products originating in the 'root' particle R decaying to the observed particle X and any Z, with variables R$(M, M_T, Y) \to$ X$(m, m_\perp, y)$ + Z [238]:

$$\frac{dN_X}{dm_\perp} = \frac{dN_X}{dm_\perp}\bigg|_{\text{direct}} + \sum_{\forall R \to X+Z} \frac{dN_X}{dm_\perp}\bigg|_{R\to X+2+\cdots}. \tag{8.43}$$

Only first-generation, and only two-body, decays were considered, as is appropriate for the hyperons and kaons. The decay contribution to the yield of X is

$$\frac{dN_X}{dm_\perp^2\,dy}\bigg|_R = \frac{g_R b_{RX}}{4\pi p^*} \int_{Y_-}^{Y_+} dY \int_{M_{T_-}}^{M_{T_+}} dM_T^2\,\mathcal{J}\,\frac{d^2 N_R}{dM_T^2 dY}. \tag{8.44}$$

Here, g_R and b_{RX} are the R-degeneracy and branching into X, and $p^* = \sqrt{E^{*2} - m^2}$ with $E^* = (M^2 - m^2 - m_2^2)/(2M)$, are the energy and momentum of the decay product X in the restframe of its parent R. The limits on the integration are the maximum values accessible to the decay product X:

$$Y_\pm = y \pm \sinh^{-1}\left(\frac{p^*}{m_\perp}\right),$$

$$M_{T_\pm} = M\frac{E^* m_\perp \cosh \Delta Y \pm p_\perp \sqrt{p^{*2} - m_\perp^2 \sinh^2 \Delta Y}}{m_\perp^2 \sinh^2 \Delta Y + m^2},$$

and

$$\mathcal{J} = \frac{M}{\sqrt{P_T^2 p_\perp^2 - (ME^* - M_T m_\perp \cosh \Delta Y)^2}},$$

where $\Delta Y = Y - y$.

The primary particle spectra (both those directly produced and parents of decay products) are derived from the thermal Boltzmann distribution. As discussed earlier in this chapter, in general the longitudinal flow does not significantly influence $m_\perp$ spectra. Thus it is possible, in order to simplify the evaluation of integrals, to disregard longitudinal flow and to allow spherical symmetry of the transverse flow. A second hadronization-surface 'velocity' seen in Eq. (8.39), $v_f^{-1} \equiv dt_f/dx_f$, was considered. Thus the thermal distribution of directly produced and parent particles R had the form

$$\frac{d^2 N}{dm_\perp\,dy} \propto \left(1 - \frac{\vec{v}_f^{-1}\cdot\vec{p}}{E}\right)\gamma m_\perp \cosh y \exp\left[-\gamma\frac{E}{T}\left(1 - \frac{\vec{v}\cdot\vec{p}}{E}\right)\right], \tag{8.45}$$

where $\gamma = 1/\sqrt{1 - v^2}$.
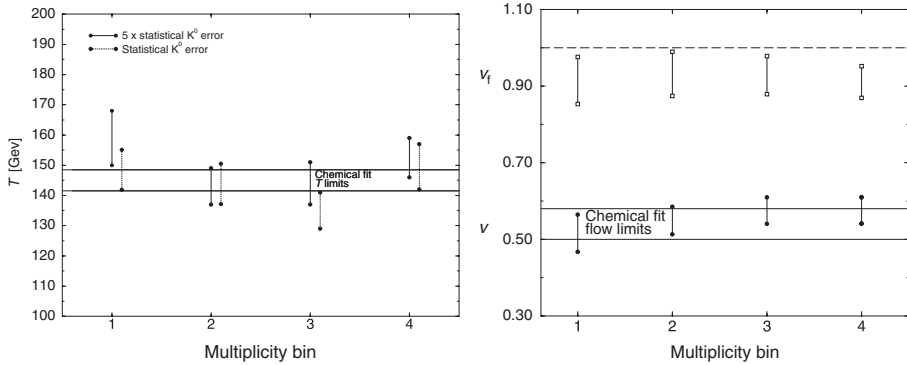
Fig. 8.12. The thermal freeze-out temperature T (left), flow velocity v (bottom right), and breakup (hadronization hyper-surface-propagation) velocity v_f (top right) for various collision-centrality bins. The upper limit $v_f = 1$ (dashed line) and chemical-freeze-out-analysis limits for v (solid lines) are also shown. For the temperature, results obtained with increased error for kaon spectra are also shown.

Simultaneous analysis of the spectra of Λ, $\overline{\Lambda}$, Ξ, $\overline{\Xi}$, $\Omega + \overline{\Omega}$, and $K_S = (K^0 + \overline{K^0})/2$ in four centrality bins was performed. In each centrality bin pronounced minima in T, v_f and v plane are observed for the total statistical error:

$$\chi^2 = \sum_i \left(\frac{F_i^{\text{theory}} - F_i}{\Delta F_i} \right)^2,$$

evaluated relative to the experimental precision of measurement ΔF_i of the result F_i. The chemical parameters, which are not well determined by a momentum-distribution fit, are not varied. Since the statistics of kaons was very high, and thus the statistical precision of data potentially was significantly greater than systematic error, also a global fit with a five-fold-increased kaon error was performed [259].

Some of the resulting $m_\perp$ spectra for particles are shown, in Fig. 8.11, in each part for the four bins separately. On the left-hand side, we see as an example the Λ spectrum. The description of the shape, in all four centrality cases, is very satisfactory, also for all other particles considered, except for $\Omega + \overline{\Omega}$ in the right-hand panel in Fig. 8.11. In all four centrality bins for the sum $\Omega + \overline{\Omega}$, the two lowest $m_\perp$ data points are underpredicted. This low-$m_\perp$ excess explains why the inverse $m_\perp$ slopes for Ω and $\overline{\Omega}$ are reported to be smaller than the values seen for all other strange (anti)hyperons in Fig. 8.10. This behavior suggests that soft Ω and $\overline{\Omega}$ are produced in a significant manner by mechanisms beyond the statistical model, which we discuss further at the end of section 19.3.

The parameters shaping the spectral form, which arise in this description of hyperon $m_\perp$ spectra, are shown in Fig. 8.12, on the left-hand side the thermal freeze-out temperature T_{tf}, and on the right-hand side the transverse velocity v (bottom) and the breakup (hadronization) speed parameter v_{f} (top). The value of v_{f} is near to the velocity of light, which is consistent with the picture of a sudden breakup of the fireball. The horizontal lines delineate the ranges of the result of chemical particle-yield analysis, and are similar to those presented in table 19.3 on page 360. The range of values of T seen in this table is slightly different as the results presented were updated. The $m_\perp$-spectral-shape analysis is found to be consistent with the purely chemical analysis of strange and non-strange hadron production.

An important objective of this complex analysis is to see whether different centrality bins yield results consistent with the same physics. There is no indication, in the left-hand panel of Fig. 8.12, of a significant or systematic change of T with centrality, or dominance of the result by the kaon spectrum alone. The resulting temperature, here dominated by the thermal shape, agrees with the temperature obtained from analysis of particle yields alone, table 19.3, which is dominated by the chemical freeze-out temperature.

The flow (expansion) velocity v (lower part of the right-hand panel of Fig. 8.12), even though it is flat to within the experimental error, reveals a slight but systematic increase with centrality, and thus size of the system. This is expected, since the more central events involve a greater volume of matter, which allows more time for the development of the flow.

For all four centralities these results show that there is no need to introduce a two-staged freeze-out; in fact, we can conclude that $T_{\mathrm{tf}} \simeq T_{\mathrm{f}}$. The myth of unequal thermal and chemical freeze-out temperatures is rooted in the high temperature obtained in chemical-*equilibrium* analysis of hadron yields. However, results of such an analysis of the experimental data lack the required statistical confidence, even though the systematic behavior of the particle production data is well reproduced, as we shall discuss at the end of section 9.2. Specifically, once a fully descriptive set of parameters is introduced, allowing for precise data description, thermal and chemical freeze-out conditions are found to be the same.

The results of the analysis described in this section are consistent with strange hadrons being produced by the new state of matter at CERN in all centrality bins explored by the experiment WA97, i.e., for numbers of participants greater than $\simeq 100$. The low-centrality fifth bin, now being studied by experiment WA57, see Fig. 9.5 [87], exhibits different characteristics, with less enhancement of the production of multistrange hadrons.
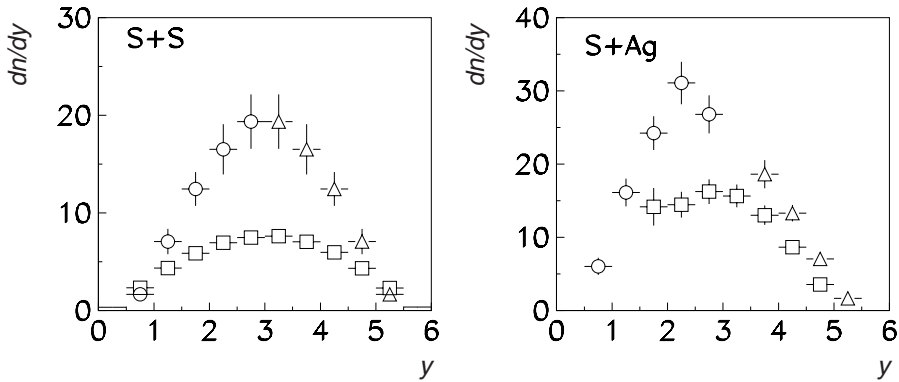
Fig. 9.1. The abundance of $1.6\Lambda + 4K_S + 1.6\overline{\Lambda}$ as a function of rapidity. On the left, S–S; on the right, S–Ag (open circles are the directly measured data). The triangles are reflected data points for S–S and reflected interpolated data employing S–S and S–Ag. The squares in the S–S case are the results for N–N collisions scaled up by the pion-multiplicity ratio; for S–Ag these are the scaled-up p–S results. Data courtesy of the NA35 collaboration [128].

9 Highlights of hadron production

9.1 The production of strangeness

Strangeness is a valuable tool for understanding the reaction mechanism, since it has to be made during the collision. The question is that of how it is produced. In terms of experimental information, the first thing we would like to establish is whether the mechanism producing strangeness involves a hot fireball at central rapidity, or whether perhaps a lot of strangeness originates from the projectile/target-fragmentation region.

Results of the experiment NA35 [128] are shown in Fig. 9.1 as functions of rapidity for the case of S–S $200A$-GeV collisions. We consider the overall abundance of $\langle s + \bar{s} \rangle$. The open circles are the measured data points, the open triangles are the symmetrically reflected data points, and squares on the left-hand side are the results of N–N (isospin-symmetric nucleon–nucleon) collisions scaled up by the ratio in pion multiplicity, whereas on the right-hand side the p–S results are scaled up. We show the rapidity yield obtained by integrating the transverse-mass $m_\perp$ distribution for the total yield of strangeness:

$$\frac{d\langle s + \bar{s} \rangle}{dy} = 1.6 \frac{d\Lambda}{dy} + 4 \frac{dK_S}{dy} + 1.6 \frac{d\overline{\Lambda}}{dy}. \tag{9.1}$$

We note that, on doubling the K_S yield, we include K_L, and, on doubling again, we add both K^+ and K^-, which explains the factor 4.